Materials for Renewable and Sustainable Energy (2024) 13:81–96
https://doi.org/10.1007/s40243-023-00253-4

ORIGINAL PAPER

Influence of the 3D architecture and surface roughness of SiOC anodes on bioelectrochemical system performance: a comparative study of freeze-cast, 3D-printed, and tape-cast materials with uniform composition

Pedro Henrique da Rosa Braun[1] · Anne Kuchenbuch[2] · Bruno Toselli[1,3] · Kurosch Rezwan[1,4] · Falk Harnisch[2] · Michaela Wilhelm[1]

Received: 5 October 2023 / Accepted: 28 December 2023 / Published online: 5 February 2024

Abstract

3D-printed anodes for bioelectrochemical systems are increasingly being reported. However, comparisons between 3D-printed anodes and their non-3D-printed counterparts with the same material composition are still lacking. In addition, surface roughness parameters that could be correlated with bioelectrochemical performance are rarely determined. To fill these gaps, slurries with identical composition but different mass fractions were processed into SiOC anodes by tape-casting, freeze-casting, or direct-ink writing. The current generation was investigated using electroactive biofilms enriched with *Geobacter* spp. Freeze-cast anodes showed more surface pores and the highest surface kurtosis of 5.7 ± 0.5, whereas tape-cast and 3D-printed anodes showed a closed surface porosity. 3D-printing was only possible using slurries 85 wt% of mass fraction. The surface pores of the freeze-cast anodes improved bacterial adhesion and resulted in a high initial (first cycle) maximum current density per geometric surface area of 9.2 ± 2.1 A m^{-2}. The larger surface area of the 3D-printed anodes prevented pore clogging and produced the highest current density per geometric surface area of 12.0 ± 1.2 A m^{-2}. The current density values of all anodes are similar when the current density is normalized over the entire geometric surface as determined by CT-scans. This study highlights the role of geometric surface area in normalizing current generation and the need to use more surface roughness parameters to correlate anode properties, bacterial adhesion, and current generation.

Keywords Microbial electrochemical technologies · Polymer-derived ceramics · 3D printing · Direct-ink writing · Freeze-casting · *Geobacter*

Abbreviations

Azo	Azodicarbonamide
BES	Bioelectrochemical system
BET	Brunauer–Emmett–Teller method
CA	Chronoamperometry
CE	Counter electrode
CT	Computed tomography
CV	Cyclic voltammetry
DIW	Direct-ink writing
EAM	Electroactive microorganisms
EET	Extracellular electron transfer
FC	Freeze-casting
GSA	Geometric surface area measured using vernier caliper
GSA-CT	Total geometric surface area measured from CT-scans
H44	Methyl phenyl silsesquioxane
HPLC	High-performance liquid chromatography
Imi	Imidazole
KS75	Graphite
MET	Microbial electrochemical technologies
MK	Methyl silsesquioxane
MFC	Microbial fuel cells

✉ Michaela Wilhelm
mwilhelm@unibremen.de

[1] Advanced Ceramics, University of Bremen, Am Biologischen Garten 2, IW3, 28359 Bremen, Germany

[2] Department of Microbial Biotechnology, Helmholtz-Centre for Environmental Research GmbH-UFZ, Permoserstraße 15, 04318 Leipzig, Germany

[3] Department of Mechanical Engineering, Federal University of Santa Catarina, Florianopolis 88040-900, Brazil

[4] MAPEX-Center for Materials and Processes, University of Bremen, Am Fallturm 1, 28359 Bremen, Germany

PDC	Polymer-derived ceramic
PBS	Phosphate buffer solution
RE	Reference electrode
SEM	Scanning electron microscopy
SSA	Specific surface area
TC	Tape-casting
TRFLP	Terminal restriction fragment length polymorphism
Volume-CT	Volume measured from CT-scans
WE	Working electrode

Symbols

A	Contact area of the anode in two-probe resistance measurement, m^2
A_{Print}	Area of the grid on the first layer of 3D-printed anode, m^2
CE	Coulombic efficiency, %
F	Faraday constant, 96,485.3 C mol^{-1}
i	Current generated during acetate oxidation, A
j_{GSA}	Current density normalized by the geometric surface area, A m^{-2}
j_{GSA-CT}	Current density normalized by the total geometric surface area, A m^{-2}
L_{Print}	Perimeter of the grid on the first layer of 3D-printed anode, m
L	Length of the anode in two-probe resistance measurement, m
Pr_i	Printability index, m^2 m^{-2}
Q	Actual charge derived from acetate consumption, C
Q_{total}	Theoretical charge derived from acetate consumption, C
R	Resistance of measured in 2-point probe method, Ohm
$2Rs_{Hg}$	Average pore diameter from Hg intrusion measurement, m
S_A	Surface arithmetical mean height, µm
S_{KU}	Surface kurtosis, 1
t	Time over acetate consumption, s
V	Volume, L
z	Number of transferred electrons, 8
σ	Electric conductivity, S cm^{-1}
Δc	Variation of acetate concentration, g L^{-1}

Introduction

Microbial electrochemical technologies (MET) are proposed as an environmentally friendly solution that combines metabolic processes (i.e., conversion of ingredients/chemicals) with the generation, storage, and utilization of electric energy [1–3]. In primary MET, whose devices are referred to as bioelectrochemical systems (BES), electric energy is harvested using electroactive microorganisms (EAM). EAM perform extracellular electron transfer (EET) to or from an electron conductor (i.e., electrode) [4]. EAM can exchange electrons with electrodes through one or more EET mechanisms, namely a) indirect EET by redox mediators, b) direct long-distance EET using cellular appendages (e.g., nanowires) for physical contact between EAM and the electrode, or c) direct EET through redox proteins present on the surface of EAM cells [5]. The primary MET archetype is the microbial fuel cell (MFC), which harvests electric energy from the purification of wastewater. To date, the range of applications of MFC is limited due to their low power density [6, 7]. At the same time, using sensors based on primary MET is very promising [8].

In most primary MET, the microbial anode is a crucial element. It consists of the electron conductor (often referred to as the "anode" or "anode material") to which the EAM adhere and grow as a biofilm while realizing the EET. The inherent properties (e.g., electronic conductivity and biocompatibility), surface chemistry, and surface area of the material used as anode are essential. Therefore, utilizing different materials or optimizing their structure are strategies to boost the performance of microbial anodes and, consequently, the power output of the MFC. Carbon-based anodes are commercially available and have been widely studied in the form of cloth, paper, plate, etc. [9, 10]. Alternative stainless steel or titanium anodes exhibit higher electric conductivity but are costly and even less corrosion resistant, and their surface usually provides poor EAM adhesion [11, 12]. Conductive polymer-based composites such as graphite felt-polyaniline or carbon paper-polypyrrole are also studied [13]. Regardless of the type of material used as the anode, one of the major challenges in increasing power density is to provide a larger surface area for the EAM adhesion while avoiding pore clogging, which limits the mass transport within the electrodes [14]. One efficient approach is to use 3D-printing technologies that can controllably increase the pore size (i.e., the distance between printed filaments) from a few micrometers to millimeters [15–18], thereby increasing the available surface area for EAM adhesion. Various 3D-structured anodes, such as layer-corrugated carbon or 3D-printed anodes made of graphene, titanium, or polylactic acid, have been reported in the literature [19–22]. Most of these studies report that pore sizes > 500 µm are the most efficient for biofilm growth without local acidification or pore clogging. In addition to biomass growth, the initial attachment of microbial cells, which determines the lag time, is also of great interest. Champineux et al. [23] describe in detail how the topography (i.e., roughness) of the anode surface (on the micro- and nano-scale) strongly influences the initial microbial cell attachment [23, 24]. In addition, other

work has found a clear influence of surface parameters on microbial cell attachment [25].

Different methods, like replica or direct foaming, are available for creating different pore sizes and morphologies. In this context, the templating method freeze-casting allows the generation of pore sizes in the range of 1 to 200 µm by adjusting the freezing rate/temperature and different porosities by adjusting the volume fraction of the solvent used (i.e., the template medium) [26, 27]. In contrast, larger pores of more than 200 µm can be printed using the 3D-printing technique (3DP) direct-ink-writing (DIW), which requires a slurry with a shear-thinning behavior that can be achieved by simply adjusting the rheological properties (e.g., yield point) [28, 29]. The starting point of this work is that we have demonstrated the successful formation of *Geobacter* spp. enriched biofilm on a tape-cast polymer-derived ceramic (PDC)-based anode with graphite and carbon black [30]. PDCs are a special class of ceramics formed from preceramic polymers with Si-based polymeric chains. Apart from the typical Si-based backbone, the preceramic polymers are varied by the additional element (X) in the backbone. Common examples of preceramic polymers are siloxanes (X=O), carbosilanes (X=C), or silazanes (X=N), where the Si atoms often carry additional functional groups such as –H, $–CH_3$, –Ph, $–CH_2=CH_2$. Using preceramic polymers allows the use of different plastic-shaping techniques like tape-casting (TC) [31], freeze-casting (FC) [32] or DIW [33]. In addition, processing preceramic polymers allows the incorporation of various carbon-based fillers like graphite, carbon nano-tubes or carbon black [34, 35]. After shaping, the preceramic polymer is cross-linked and later heat-treated at low temperatures (< 1000 °C) using an inert gas atmosphere [36]. By controlling the pyrolysis temperature (i.e., the conversion of the preceramic polymer into a ceramic) the surface area, porosity, and hydrophilicity of the final SiOC can be tuned [37]. When processing polysiloxane with carbon-based fillers, the electric properties in SiOC are enhanced by the formation of percolation paths through carbon that decrease the electric resistance. Therefore, a corrosion resistant, porous, chemically stable, and electric conductive SiOC can be formed [37, 38]. In the investigation of different PDC variants, biofilms dominated by *Geobacter* spp. were used. These species are the archetypal EAM that perform direct EET during the formation of biofilms. These biofilms can be obtained by electrochemical selection, allowing fair cross-comparison and benchmarking between different anode materials [4, 39].

In this work, electric conductive PDC anodes of the same material composition were produced by different manufacturing processes (TC, FC, DIW), for which the yield point of the used slurry had to be adapted in each case. In addition to analyzing the pore structure and the physiochemical properties of the anodes, the resulting surface roughness and the geometric surface (GSA) were characterized from a broader perspective using the surface roughness kurtosis parameter and the total geometric surface area from CT scans (GSA-CT), respectively. With these anode materials, we also studied how the altered surface and roughness effect biofilm formation as well as composition, and consequently, the resulting current density (j_{GSA} or $j_{GSA\text{-}CT)}$ as well as coulombic efficiency (*CE*). This is followed by a brief discussion of the different methods used to determine the geometric surface and the resulting current density, which is compared with work from the literature. Finally, the current density generated from the anodes in this study is compared with that of other works using biofilms enriched with *Geobacter* spp. as EAM.

Experimental section

Chemicals for anode fabrication

The SiOC anodes were prepared by tape-casting, direct-ink writing, or freeze-casting using a slurry composed of poly (methyl silsesquioxane) (MK, Silres® MK, Wacker Chemie AG) and poly (H44, methyl phenyl silsesquioxane) (Silres® H44, Wacker Chemie AG) as preceramic precursors. Graphite (KS75, IMERYL Graphite and Carbon) and carbon black (Vulcan XC72 Cabot) were added to improve the electric conductivity based on previous works [30]. Azodicarbonamide (Azo, azodicarbonamide Sigma- Aldrich Co) and Molybdenum disilicide ($MoSi_2$, abcr GmbH) were added as fillers to induce the formation of pores and to control the shrinkage, respectively. Additionally, imidazole (Imi, Alfa Aesar) was used as a cross-linking catalyst. Together, these components formed the solid fraction, which is described in Table S2. *p*-xylene (Sigma-Aldrich) was used as solvent for the mixture of precursors and fillers. The mass fraction of the samples was calculated taking into account the solid fraction.

Preparation of the slurries

First, the solid components such as the preceramic precursors (MK and H44), the carbon-based conductive phases (graphite and carbon black), Azo, and $MoSi_2$ were ball-milled for 24 h with 90 rpm to ensure homogenous mixing of the components. The proportion of the volume of the chemicals, the milling balls (alumina $D_{50} = 9.70 \pm 2.0$ mm) and the empty space in a 1 L bottle was 1:1:1. The solid components were then mixed with the solvent at room temperature using a magnetic stirrer for slurries with a mass fraction of 70.8 wt% or a mechanical stirrer at a mixing speed of 200 rpm for slurries with mass fraction of 85 wt%. After 30 min of mixing, the cross-linking agent, Imidazole, was added while stirring at the same mixing speed for more

30 min. The mass fraction was controlled by monitoring the evaporation of solvent mass (i.e., weighting the total mass of the slurry) during the mixing of all chemicals and the subsequent mixing time for homogenization. Thus, the slurries with more solid loading had less solvent mass, and the slurries with less loading had more solvent mass (Table 1).

Tape-casting, freeze-casting and direct-writing of the slurries

Tapes were produced using a tape-casting process with an adjustable gap doctor blade, followed by a drying step for 24 h at room temperature. For the freeze-casting process, the slurries were frozen in a mold at −20 °C using a unidirectional single source cold finger device as described elsewhere [40]. After 1 h, the frozen anodes were transferred to a freeze-dryer for 72 h at 20 °C and 10 µbar. For the direct-ink writing process the slurries were filled into 3 mL cartridges from Nordson (Erkrath, Germany). A pneumatic-based extrusion printer (Cellink INKREDIBLE® 3D) using conical precision tip nozzles (nozzle inner diameter of 610 µm) from Techcon (Eastleigh Hampshire, UK) was used for 3D printing with an air pressure of 130 ± 15 kPa, that was monitored and controlled manually when necessary. The cartridges were placed inside a recipient with a saturated-solvent atmosphere before attaching to the 3D printer to avoid solvent evaporation. The anodes were printed at 10 mm/s in lattice cuboid-shape (smallest unit 1.5 × 1.5 × 0.5 mm) with a 90° grid and 1 mm spacing between filaments. The numerical code with the printing commands was generated using the Cellink Heartware 2.4.1 software, with a 33% infill density (solid volume in the printed component). Later, the 3D-printed anodes were dried at room temperature for 24 h. Regardless of the fabrication method, all anodes were stored at room temperature after fabrication/ prior to heat treatment. The anodes were then converted to ceramics through pyrolysis at 1000 °C under a pure nitrogen atmosphere (purity 99.999%). The heating rate up to 900 °C was of 120 K h^{-1}, followed by 30 K h^{-1} up to 1000 °C. The dwelling time lasted 4 h and the cooling rate to room temperature was 120 K h^{-1}. All anodes were made with a rectangular shape (Fig. 1).

Table 1 Denotation, mass fraction and processing method of the anode materials

Denotation	Mass fraction, wt%	Processing method
TC_70.8%	70.8	Tape-casting
TC_85%	85	Tape-casting
FC_70.8%	70.8	Freeze-casting
3DP_85%	85	Direct-ink writing

Materials characterization

The yield point and the thixotropy of the slurries were characterized by a stress-controlled rotational rheometer, Kinexus Pro (Malvern Panalytical, Kassel, Germany). For both tests, roughly 20 mL of the slurry was placed at a distance between the base plate of the rheometer and a parallel plate with a diameter of 20 mm at a gap of 1 mm. All measurements were performed at a controlled temperature of 25 °C using a solvent trap to avoid evaporation of the solvent. The yield point was obtained from a triplicate of measurements using a continuous shear rate ramp from 0.01 to 1000 s^{-1}. The thixotropy of the slurry was analyzed by a three-step shear rate test with the first step at 0.05 s^{-1}, the second step at 50 s^{-1}, and the last step at 0.05 s^{-1}. The first and second steps lasted 60 s, and the last step 120 s. The quality of the print of the slurry was evaluated by first taking pictures from the top of the pyrolyzed anodes with a digital optical microscope (VHX-5000 from Keyence, Neu-Isenburg, Germany). Then, from the images of the first layer, the perimeter and the area between the filaments were analyzed using ImageJ software [41]. With these values, the printability index Pr_i which characterizes the quality of the print [42] was calculated according to the Eq. (1):

$$Pr_i = \frac{(L_{Print})^2}{16A_{Print}} \quad (1)$$

where Pr_i is the printability index factor, L_{Print} is the perimeter of the squared hole and A_{Print} is the area of the squared hole. A Pr_i equal to 1 indicates a perfectly squared grid, whereas values higher or lower than 1 indicate irregular or circular holes, respectively [43]. The pore structure of the anodes from the cross-section and the top view, before and after the BES experiments, was analysed with a scanning electron microscope (SEM, Zeiss EVO 10, Carl Zeiss Microscopy GmbH, Zena, Germany) using specimens sputtered with gold (K550, Emitech, Judges Scientific Plc., West Sussex, UK). The distribution of the pore's diameter size, the average pore diameter ($2Rs_{Hg}$), and the open porosity were determined by Hg intrusion porosimetry (Pascal 140/440, POROTEC GmbH, Haan, Germany). Nitrogen adsorption isotherms at 77 K were recorded and analyzed (Belsorp-Mini, Bel Japan Inc.) to evaluate the specific surface area (SSA) of the anode materials according to Brunauer- Emmett-Teller (BET) method. Prior to this measurement, a representative piece of a single SiOC electrode of each composition was ground and sieved (particle diameter < 300 µm). The resulting powder was then inserted into the glass cell, and preheated at 120 °C for 3 h under vacuum. The hydrophilicity of the anodes was analyzed by calculating the ratio between the mass uptake of water and *n*-heptane vapor. For this analysis, another representative

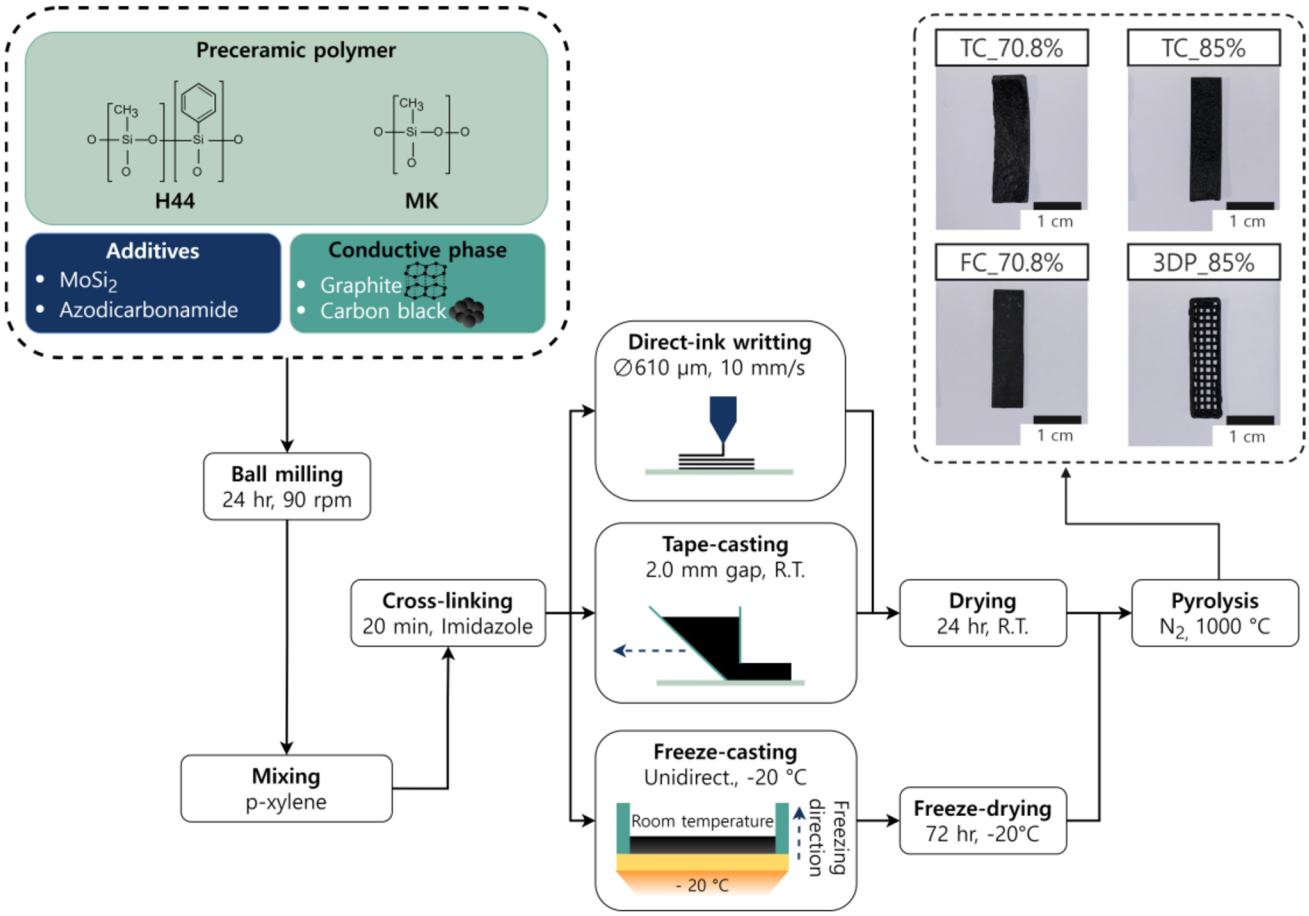

Fig. 1 Flowchart of the different processes (direct-ink writing, tape-casting and freeze-casting) for the production of SiOC anodes. On top right: light microscopy images of all anodes

piece from each composition was ground, sieved (particle diameter < 300 µm), placed in a glass vial (with an open lid), and dried at 70 °C for 24 h. The dried powder (inside the glass vial) was then placed in a closed Erlenmeyer flask partially filled with water of *n*-heptane at 20 °C. After 24 h, the powders were removed from the Erlenmeyer flask and weighted to determine the vapor uptake. The geometric surface area (GSA) of the anodes was measured using a vernier caliper. The total geometric surface area (GSA-CT) and the total volume (volume-CT) were determined by reconstructing CT scans of the entire anode. In the case of 3D-printed anodes, this total geometric surface area also considers the external surface area within the grid structure. The CT scans measurements were done using X-ray micro-computed tomography (µ-CT) Xradia 520 Versa device (Carl Zeiss Microscopy GmbH, Jena, Germany). For this analysis, one anode from each composition was scanned. The X-ray micro-computed tomography scanning parameters and specifications and a picture of the reconstructed spatial representation of all anodes are described in Table S1 and Figure S1, respectively. CT scans were first binarized from grayscale to black-and-white images using the Otsu threshold filter in ImageJ software [41]. The binarized images were then reconstructed as a 3D spatial representation from the binary CT scans and the calculation of the GSA-CT and volume-CT was done by software 3D Slicer [44]. The chemical stability of the anodes was evaluated by the dry weight variation in a phosphate buffer solution (PBS, pH 7,) over a period of 4 weeks. For this analysis, one anode from each composition was used, and the dry weight was measured every 7 days. The resistance was measured at 20 °C using an electrometer (Keithley 197, Keithley Instruments, United States of America). The two ends of the anode were polished and placed (i.e., sandwiched) between two copper plates for resistance measurements. The electric conductivity was calculated as it follows:

$$\sigma = \frac{L}{R \times A} \tag{2}$$

where σ is the electric conductivity, R is the measured resistance, and L and A are the length and the contact area of the anode, respectively. The spatial surface roughness of the

anodes was analyzed with an optical profilometer (Plμ2300, Sensofar, Barcelona, Spain) and the software Sensomap Plus 5.0, with parameters calculated according to ISO25178. Two spatial parameters that deviate significantly from anode to anode namely, arithmetical mean height (S_A) and kurtosis (S_{KU}) were selected for comparison. S_A expresses the height difference of each point compared to the arithmetical mean of the surface and S_{KU} is the measure of the sharpness of the roughness profile (skewed or spiked) [23, 25, 45, 46]. Three different regions of one anode from each anode variant were evaluated. All experimental parameters, i.e. voltage and magnification, were kept constant during data acquisition.

Bioelectrochemical experiments

Bioelectrochemical experiments were conducted for 32 days in three-electrode bioelectrochemical systems (BES) consisting of glass bottles (DWK Life Sciences, Wertheim, Germany) with a total working volume of 250 mL. Different PDC materials (TC_70.8%, TC_85%, FC_70.8%, and 3DP_85%) were studied as anodes acting as working electrodes (WE). The values for GSA and GSA-CT of these anodes, to which the current density referred, are listed in Table 2. Each of these anodes was studied in triplicates, resulting in a total of 12 individual BES running in parallel. A graphite rod (CP Handels GmbH, Wachtberg, Germany) with a GSA of 17.2 cm^2 and a Ag/AgCl sat. KCl, + 0.197 V vs. SHE (SE 11, Xylem Analytics Germany Sales GmbH & Co. KG Sensortechnik Meinsberg, Germany) were used as the counter electrode (CE) and reference electrode (RE), respectively. The WE and CE were connected to the potentiostat via stainless steel wire (Ø 0.6 mm, Goodfellow, Cambridge, England). In the case of the WE, a conductive carbon cement (Leit-C, Plano GmbH, Germany) and an epoxy resin were used to insulate and to attach the stainless steel wire to the WE. All electrodes were assembled in a butyl rubber stopper and previously chemically sterilized (70% Ethanol, 100 mM H_2SO_4).

The medium used in the BES was prepared according to [47], supplemented with sodium acetate (10 mM) that acted as the sole carbon source and electron donor. Prior to the start of the experiment, the medium was purged with nitrogen for 30 min to ensure anaerobic conditions. After 3 h of electrochemical abiotic operation (+ 0.2 V vs. Ag/AgCl sat. KCl), the BES were inoculated with secondary *Geobacter* spp. enrichment biofilm gained as described elsewhere [48] and operated under batch conditions. All experiments were carried out under anaerobic conditions and potentiostatic control using a multi-channel potentiostat/galvanostat (MPG-2, Bio- Logic Science Instruments, Claix, France). The BES were chronoamperometrically (CA) operated at a potential of + 0.2 V vs. Ag/AgCl sat. KCl for 32 days at 32.5 °C (Incubator Hood TH 15, Edmund Bühler GmbH, Bodelshausen, Germany) and constantly stirred at 120 rpm (2mag, München, Germany).

The medium of all BES was replaced when the current production from at least one of the experimental setups dropped to values close to zero, representing a feeding cycle. To ensure the anaerobic conditions during the medium exchange, an air-tight overpressure system was used, and the medium was continuously flushed with nitrogen. All chemicals used for the bioelectrochemical experiments were of analytical grade and supplied by Carl Roth GmbH (Karlsruhe, Germany) and Merck KGaA (Darmstadt, Germany). Deionized water (Merck Chemicals GmbH, Darmstadt, Germany) was used to prepare all solutions.

Analytical methods and calculation

The acetate concentration was monitored using high-performance liquid chromatography (HPLC, Shimadzu Scientific Instruments, Kyoto, Japan) measurements of the aqueous liquid phase with a refractive index detector (RID-10 A, Shimadzu Scientific Instruments, Kyoto, Japan). A Hi-Plex H-column (300 mm × 7.7 mm ID, 8 µm pore size, Agilent Technologies, Santa Clara, USA) was used, and the column was equipped with a precolumn (Carbo-H 4 mm × 3 mm ID, Security Guard, Torrance, Phenomenex, Torrance, USA). Isocratic elution at 50 °C with 5 mM of H_2SO_4 was set at 0.5 mL min^{-1} for 30 min. Peak identification and calibration of acetate was carried out with external standards ($R^2 > 0.99$). The medium was sampled before and after its replacement (in each feeding cycle), centrifuged at 13,000 × g for 5 min, and filtered with a 0.2 µm nylon filter.

The acetate consumption data were used to determine the coulombic efficiency *CE*. By dividing the actual charge generated *Q* (Eq. 3) and the theoretical charge from acetate oxidation Q_{total} (Eq. 4) (calculated assuming that all substrate consumed is converted to electricity), one obtains the *CE*

Table 2 Denotation, geometric surface area (GSA), GSA-CT, volume and volume-CT

Denotation	GSA, $cm^2 \pm cm^2$	GSA-CT, cm^2	Volume, cm^3	Volume-CT, cm^3
TC_70.8%	4.25 ± 0.3	5.89	0.396 ± 0.03	0.406
TC_85%	4.64 ± 0.1	6.14	0.432 ± 0.01	0.439
FC_70.8%	3.87 ± 0.1	4.03	0.359 ± 0.01	0.366
3DP_85%	5.01 ± 0.1	12.33	0.567 ± 0.01	0.276

(Eq. 5). Q is the produced charge derived from the integration of current (i) over time (t):

$$Q(t) = \int_0^t i\, dt \tag{3}$$

Q_{total} is the theoretical charge derived from acetate consumption determined by HPLC analysis.

$$Q_{\text{total}} = \Delta c \times V \times z \times F \tag{4}$$

Δc is the change in acetate concentration, V is volume, z is the number of transferred electrons (8 in case of acetate), and F is the Faraday constant (96,485.3 C mol^{-1}). Subsequently the CE can then be calculated:

$$CE = \frac{Q}{Q_{\text{total}}} \times 100\% \tag{5}$$

The maximum current density normalized to the geometric surface area (j_{GSA}) was calculated by dividing the maximum current generated by the GSA. In the same way, the maximum current density normalized by the total geometric surface area ($j_{\text{GSA-CT}}$) was calculated by dividing the maximum current generated by the GSA-CT.

Microbial analysis

The microbial community composition of bacteria and methanogenic archaea on the DNA level was analyzed using standard terminal restriction fragment length polymorphism (TRFLP). The results are expressed as the relative amplicon abundance of each terminal restriction fragment (~ taxon), ranging from 0 to 100% or presented in fractions, from 0 to 1 (as in this paper). For this purpose, parts of the reddish biofilms formed on the surface of the anodes were sampled by scraping the microbial material with a sterile needle. The DNA extraction was performed with the NucleoSpin® Soil Kit (Macherey- Nagel, Germany) following the manufacturer's instructions. Finally, the gDNA was eluted in 50 µL of elution buffer and the concentration was measured with the Nano Drop™ One (Thermo Fisher Scientific, USA). The microbial community was analyzed using the primers UniBac27f (FAM labelled), and the primer Univ1492r to amplify the partial sequence of the 16S rRNA gene of bacteria [49]. mlas and mcrA rev (FAM labeled) were used for amplifying the archaeal *mrcA* gene (subunit A of methyl coenzyme M reductase) [50].

The Polymerase Chain Reaction (PCR) (Master Mix) contained 6.25 µL of enzyme mix (MyTaq HS Red Mix, 2×, Bioline, Germany), 0.25 µL of each primer (5 ρmol μL^{-1}, supplied by MWG Biotech, Germany), 4.75 µL of nuclease-free water, and 1 µL of genomic DNA (in general about 20 to 25 ng). The PCR cycle parameters were as follows for 16 s rRNA genes of bacteria: 1 min at 95 °C, 25 cycles of 15 s at 95 °C, 15 s at 54 °C, and 2 min at 72 °C, followed by a 10 min extension step at 72 °C [51]. The parameters for the *mcrA* genes were: 1 min at 95 °C, 5 initial cycles of 15 s at 95 °C, 15 s at 48 °C and 30 s at 72 °C, including a ramp rate of 0.1 °C s^{-1} from the annealing to the extension temperature, 25 cycles of 15 s at 95 °C, 15 s at 52 °C, and 30 s at 72 °C followed by a 10 min extension step at 72 °C [52]. The PCR products were purified (SureClean Plus, Bioline), quantified (Qubit® Fluorometer 3.0 and Qubit® dsDNA HS Assay Kit, Life Technologies, USA). Then 10 ng were digested with restriction endonucleases *Hae*III for the 16S rRNA genes of bacteria and *Mwo*I for *mcrA* of methanogenic archaea (New England Biolabs, Germany). After product precipitation (EDTA/EtOH), a TRFLP analysis was performed using an ABI PRISM Genetic Analyzer 3130xl (Applied Biosystems™, USA) and Map- Marker® 1000 (BioVentures Inc., USA) for the 16S rRNA genes and Red DNA Size Standard (LAB, USA) for the *mcrA*, as a size standard.

For the analysis of the biofilms using SEM, the biofilms on the surface of the anodes were first fixed in 2.5% glutaraldehyde for 60 min and subsequently dehydrated for 10 min in alcoholic solutions of 20, 40, 60, 80 and 100% ethanol. The materials were dried and gold-coated (K550, Emitech SA, West Sussex, UK) for 20 s under an argon atmosphere.

Results and discussion

This section describes and discusses the rheological properties, pore structure, and physiochemical and functional properties of the anodes. Then, the performance of the anodes in BES is described and related to the anode properties. Finally, a genetic analysis of the microbial community structure is presented.

Synthesis and pore structure and physicochemical properties of anode materials

While the original slurry composition used already for tape-casting in previous work [30] could also be used for freeze-casting without further modification, the rheology of the slurry had to be adapted for 3D-printing. Successful printing and shape fidelity is generally achieved when the slurry (i.e., ink) exhibits a shear-thinning behavior with a significant yield point to ensure that the slurry behaves as solid in the steady state (e.g., inside the nozzle) and does not flow until a shear stress is applied [42]. The thixotropy of the slurry indicates its behavior before, during, and after printing, while the post-printing recovery indicates whether a filament regains its shear viscosity after printing. The shear rate ramp was performed to determine the onset of flow, with the arrow in Fig. 2A indicating the yield point. When this

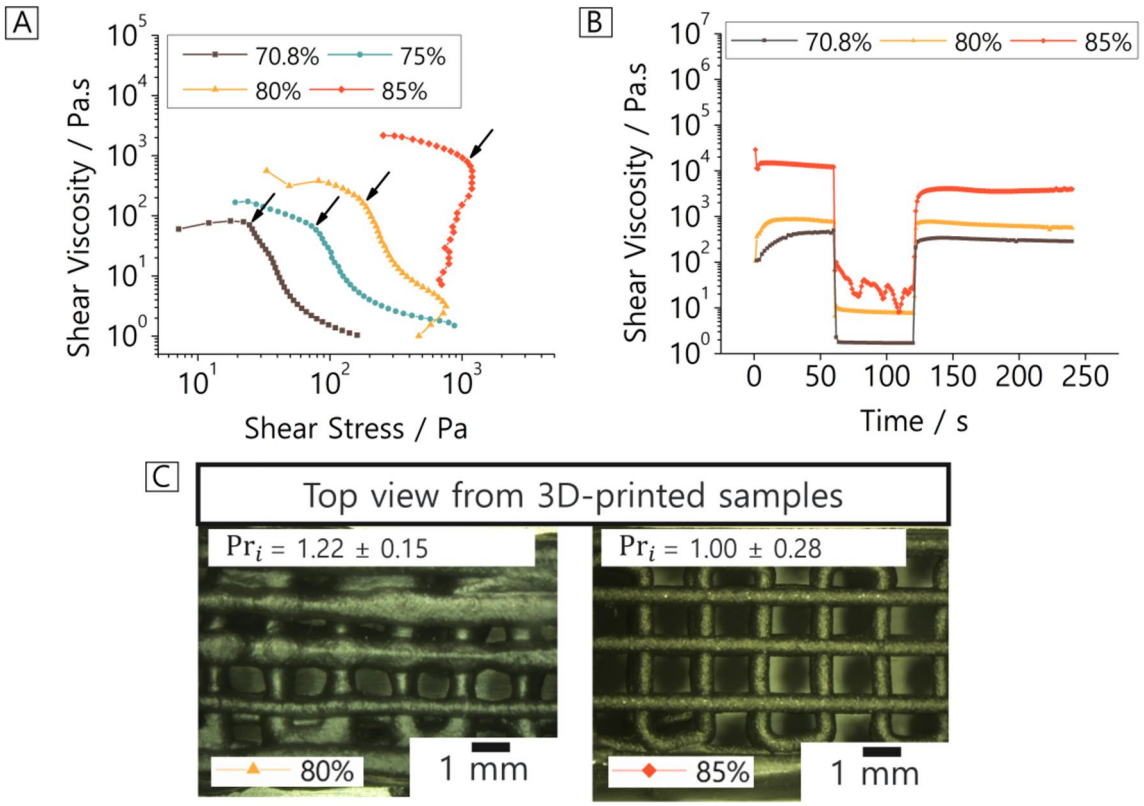

Fig. 2 **A** Shear rate ramp for slurries with mass fractions ranging from 70.8 to 85 wt%. The arrows indicate the yield point, characterized by a significant drop in shear viscosity. **B** Three-step thixotropy test for slurries with 70.8 wt%, 80 wt% and 85 wt% of mass fraction. The initial phase of the test last 60 s under a shear rate of 0.05 s^{-1} followed by 60 s under a shear rate of 50 s^{-1}, and ended with 120 s under a shear rate of 0.05 s^{-1}. **C** Optical micrography and Pr_i for 3D-printed anodes with 80 wt% and 85 wt% of mass fraction, after pyrolysis

yield point is reached, flow starts, and the shear viscosity drops steeply. It was found that increasing the mass fraction from 70.8 wt% to 85 wt% in steps of 5 wt% increased significantly the yield point from 25 to 1141 Pa.

The three-step test (Fig. 2B) shows that all slurries exhibit thixotropic behavior, regaining the high shear viscosity after a high shear rate (indicated by the renewed increase at the transition from step 2 to step 3). As the mass fraction increases, the shear viscosity of the slurry increases in each test step. Although the slurry with 70.8 wt% also shows thixotropic behavior, it was observed that this slurry already flows slowly in the nozzle before printing. When printing the slurry with 80 wt%, it was also found that the filament collapsed after a subsequent filament was printed on. Only the 85 wt% slurry provided the highest shear viscosity during all steps necessary to ensure adequate printability and filament stability. Slurries with higher mass fractions (> 85 wt%) were not developed due to the challenge of controlling the evaporation of solvent during preparation. Freeze-casting of 85 wt% anodes was not pursued because of the difficulty in ensuring that the slurry settled on the mold without trapping bubbles. In addition, the solvent could not be removed entirely in the freeze-drying process even after a longer drying time (> 72 h). After optimizing the shear viscosity of all slurries for the shaping processes, the anodes were pyrolyzed in a nitrogen atmosphere at 1000 °C. During pyrolysis, the silsesquioxanes and their organic groups are decomposed, and the carbon atoms are incorporated into the Si–O network. This process converts the preceramic polymer into an amorphous/glassy SiOC ceramic [37]. Graphite and carbon black are both forms of carbon with a layered or highly disordered structure, respectively. Graphitization occurs during pyrolysis (i.e., restructuring into a more organized hexagonal structure), especially in graphite. Both components act as conductive phases when incorporated into SiOC materials, increasing their electric conductivity [38]. Azodicarbonamide decomposes completely thermally at around 200 °C, releasing various gases (e.g., nitrogen, carbon monoxide, and carbon dioxide) that serve as blowing agents to create porosity in the anodes [53]. In an inert nitrogen atmosphere, molybdenum disilicide acts as a filler to prevent shrinkage of the anodes[54]. Imidazole, on the other hand, acts as a crosslinking catalyst,

with high degrees of crosslinking stabilizing the structure and thus increasing the ceramic yield [38].

All anodes produced were mechanically stable for handling in further tests. When analyzing the pyrolyzed 3D-printed anodes with 80 wt% and 85 wt% (Fig. 2C), the 3D-printed anodes using a slurry with 85 wt% shows a Pr_i factor of 1.00 ± 0.28 indicating a nearly perfect square-grid. In contrast, printing using a slurry with 80 wt% leads to a Pr_i factor of 1.22 ± 0.15, indicating an irregular shape grid.

The pore morphology of pyrolyzed materials was investigated in cross-section and on the surface of the anodes by evaluating SEM pictures (Fig. 3). Since high shear stress occurs on the surface of the material during shaping in the TC and 3DP processes [34, 55, 56], anodes fabricated by these processes have a dense surface layer on the top (surface view).

In contrast, in FC, the particles are stacked on to each other [57], so that the surface of the freeze-cast anode possess an open porosity, which is also a qualitative indication of a higher surface roughness.

An additional evidence of high shear stress during TC is the orientation of particles in the horizontal process direction, which was also observed by Hirao et al. on tape-cast silicon nitride [55, 58]. A quantitative overview of the pore structure of the anodes is given in Fig. 4 in terms of pore diameter size distribution, open porosity, and SSA. Most pore diameter size ranges from 0.008 to 6 µm. The small volume of pores larger than 10 µm in diameter exhibited by the anodes TC_70.8% and TC_85% may be due to a small number of internal cracks that other methods cannot detect. The tape-cast anodes show an average pore diameter $2Rs_{Hg}$ (i.e., highest volume of a pore diameter size) of 0.41 µm for TC_70.8% and 0.26 µm for TC_85%. The anode 3DP_85% has $2Rs_{Hg}$ of 0.21 µm and, similar to the tape-cast anodes, a higher relative volume of pores with a diameter below 1 µm. The anode FC_70.8% has a $2Rs_{Hg}$ of 1.9 µm and a large volume of pores with a diameter of more than 1 µm. This difference can be attributed to the arrangement of the particles, as mentioned earlier, which differs in 3DP and FC. Pores larger than 1 µm can generally improve the adhesion and growth of the EAM on the anode surface [52].

The open porosity for tape-cast and 3D-printed anodes is about 25%, while it is 34% for the freeze-cast anode. This difference between the values can again be attributed to the different particle arrangement, which varies from one shaping method to another. The SSA is a key parameter for the interaction between the anode surface and the EAM. The nitrogen adsorption and desorption isotherms are type IV, indicating the presence of meso-macropores in the anode. In this regard, the SSA values analyzed by the BET method range from 35.18 to 50.85 $m^2\ g^{-1}$ as previously observed [30]. Although the micropores of the matrix are usually destroyed during pyrolysis up to 1000 °C, the anodes still show relatively high SSA values, which can be partly attributed to the intrinsic surface area of 44.8 $m^2\ g^{-1}$ of the added carbon black. Due to the same chemical composition, no trend can be observed for the SSA values that could be attributed to the processing method or the mass fraction. Profilometric analysis shows quantitative results in terms of surface roughness, with the anodes TC_70.8% and FC_70.8% showing S_A values of 2.0 ± 0.2 and 2.3 ± 0.4 µm, respectively. In contrast, the TC_85% and 3DP_85% anodes

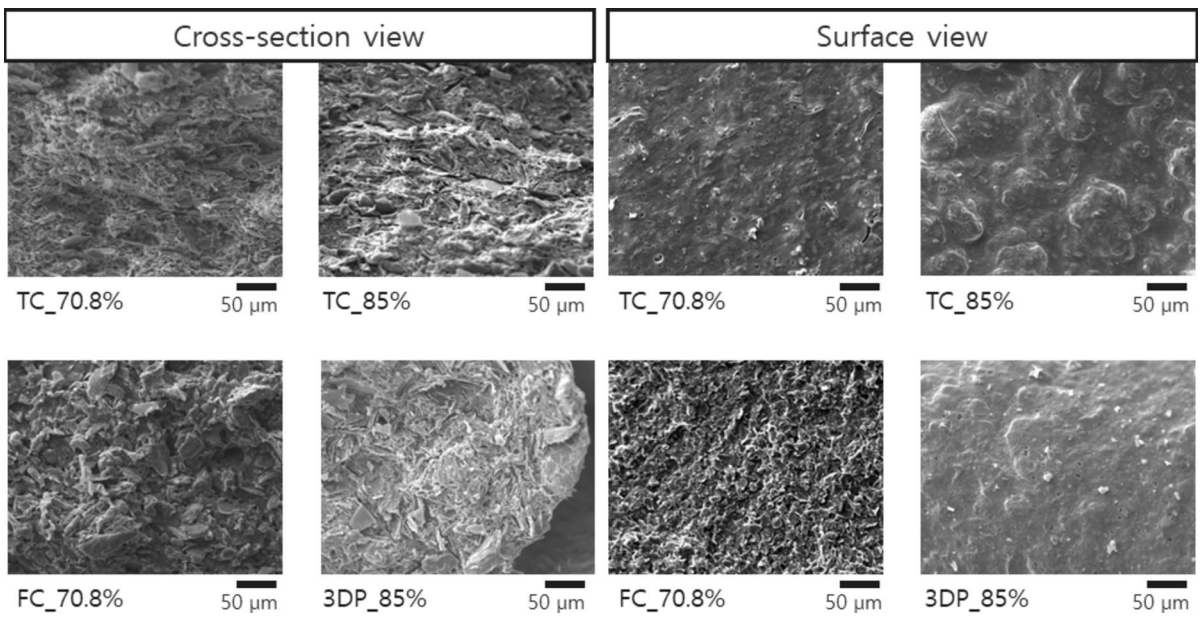

Fig. 3 SEM pictures of anode materials, before the use in bioelectrochemical systems

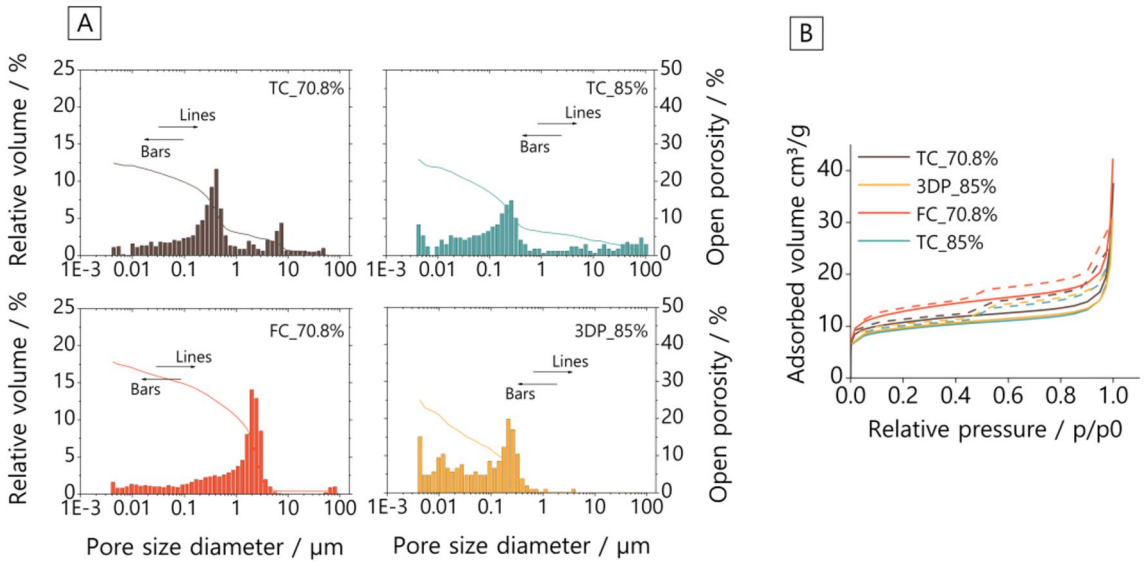

Fig. 4 **A** Pore diameter size distribution (bars) and open porosity (lines) (left) and **B** nitrogen adsorption and desorption isotherms with the dashed lines representing the desorption of nitrogen

show higher S_A values of 7.7 ± 2.7 and 6.8 ± 0.8 µm, respectively. That indicates that processing slurry with a higher mass fraction of 85 wt% results in surfaces with peaks and valleys that are further away from the average surface mean plane. The S_{KU} values of anodes TC_70.8%, TC_85% and 3DP_85% is 3.4 ± 0.3, 2.6 ± 0.7 and 3.3 ± 1.1, respectively. Only anode FC_70.8% shows higher values of S_{KU} of 5.7 ± 0.5 and indicates a sharper roughness, confirming the observations from SEM images in Fig. 3. The surface roughness values are summarized in Table 3.

Since in the literature the current density of the anode is usually related to the geometric surface area or the resulting anode volumes, these were also determined (Table 2). For the tape-cast and freeze-cast anodes, the GSAs had similar values between 3.87 ± 0.08 cm^2 and 4.64 ± 0.01 cm^2, while their volumes ranging between 0.359 ± 0.008 and 0.432 ± 0.001 cm^3. The 3D-printed sample is of the same order of magnitude with a GSA of 5.01 ± 0.01 cm^2 and a volume of 0.567 cm^3. Besides, GSA-CT and the volume-CT were calculated from the reconstruction of CT scans to obtain more approximated values for structures that, like the 3D structure, cannot be calculated using a caliper. For the FC_70.8% anode, the two surfaces or volumes do not differ. However, the GSA values of the TC_70.8% and TC_85% tape-cast anodes are smaller than their GSA-CT values, which is because, during pyrolysis, the TC_70.8% and TC_85% anodes curved slightly, which is why the length of these anodes measured with the caliper was about 7 and 11% smaller than the actual length. In contrast, the 3D-printed anode shows a more than doubled GSA-CT value of 12.31 ± 0.11 cm^2 with a significantly reduced volume-CT of 0.276 cm^3.

The electric conductivity measured by a 2-point probing method with 2 parallel copper plates varied from 4.0×10^{-2} to 1.75 S cm^{-1}, depending on the fabrication method. The direction in which the current is measured and the orientation of the pore structure created by TC and 3DP result in an anisotropic electric conductivity for these anodes [59]. However, during operation as an anode in BES at a small scale this effect might be negligible.

In measurements of the chemical stability of the anodes in PBS solution over 28 days (Fig. S2), the anodes showed a mass decay of less than 3.2%, which is consistent with results reported in the literature for PDC-based anodes (i.e., less than 5%) [38]. In addition, all anodes exhibited a water/*n*-heptane absorption ratios of about 4 (Fig. S2) and

Table 3 Denotation, j_{GSA}, $j_{GSA\text{-}CT}$, CE, S_A, S_{KU}, $2Rs_{Hg}$

Denotation	j_{GSA}, A m^{-2}	$j_{GSA\text{-}CT}$, A m^{-2}	CE, %	S_A, µm	S_{KU}	$2Rs_{Hg}$, µm
TC_70.8%	5.9 ± 1.5	4.3 ± 1.1	55.9 ± 18.8%	2.0 ± 0.2	3.4 ± 0.3	0.41
TC_85%	6.8 ± 1.5	5.1 ± 1.2	78.6 ± 47.3%	7.7 ± 2.7	2.6 ± 0.7	0.26
FC_70.8%	9.2 ± 2.1	8.8 ± 2.1	39.0 ± 19.7%	2.3 ± 0.4	5.7 ± 0.5	1.90
3DP_85%	12.0 ± 1.2	4.9 ± 0.5	89.0 ± 33.6%	6.8 ± 0.8	3.3 ± 1.1	0.21

thus hydrophilic surfaces, which are beneficial for biofilm development.

Using different manufacturing processes, it is thus possible to produce PDC anodes with the same composition and thus the same physicochemical properties. The anodes have significantly different texturing of the inner pore structure, the pore and surface sizes and also the surface roughness. How these parameters influence the growth of a biofilm and its performance was subsequently investigated.

Operation and performance of the BES

The porous anodes were tested in triplicates of independent BES using batch conditions for 32 days (Fig. S3). The maximum current density normalized by the geometric surface area (j_{GSA}) for the tape-cast anodes was 5.9 ± 1.5 A m^{-2} and 6.8 ± 1.5 A m^{-2} when using TC_70.8% or TC_85%, respectively. The freeze-cast anode (FC_70.8%) showed a j_{GSA} of 9.2 ± 2.1 A m^{-2}, while the 3D-printed anode (3DP_85%) showed the highest j_{GSA} of 12.0 ± 1.2 A m^{-2}.

We assume that the high j_{GSA} value of 3DP_85% is due to the large pores of about 1 mm (i.e., the space between the lattice structure) created by the 3D-printing, which results in a larger actual surface area than the GSA. This combination avoids fast clogging or closing of pores during operation while providing a larger area for the biofilm to form and may avoid mass-transfer limitations [16, 60]. When comparing anodes with the same composition and mass fraction, the j_{GSA} generated by the 3D architecture of the anode (3DP_85%) is 1.7 times higher than that of the flat anode TC_85%. The open surface of the anode FC_70.8% with higher S_{KU} may have more anchoring points for EAM attachment, leading to a high initial j_{GSA} of 9.2 ± 2.1 A m^{-2} in the first cycle. However, there is a subsequent drop in j_{GSA} to the range of the other "flat anodes" (TC_70.8% and TC_85%), most likely due to rapid clogging of the upper rough surface. In addition to reporting the common S_A when correlating to the anode surface, we suggest exploiting parameters like S_{KU}, as already done for bacterial adhesion [61]. To certify the reproducibility of this study, the j_{GSA} values from the sample TC_70.8% and the reference sample from the previous study [30]—which are materials produced by the same processing method and mass fraction—were compared (Fig. 5A) and the values are similar during all cycles. Cyclic voltammetry (CV) analysis was not possible, as all anodes showed a high capacity and hence background current. The coulombic efficiency (*CE*) of the tape-cast anodes with mass fraction of 70.8 wt% and 85 wt% was 55.9 ± 18.8% and 78.6 ± 47.3%, respectively, whereas for the freeze-cast anodes, the *CE* was 39.0 ± 19.7% and for the 3D-printed anodes 89.0 ± 33.6%.

The surface area used to normalize the current to obtain the current density is highly relevant when reporting electrode performance. The surface area of the anodes with a 3D architecture can often be calculated or considered differently [62]. The relevant area—also called the electroactive area or microbially accessible area—that is exposed to and colonized by the biofilm is important but cannot be

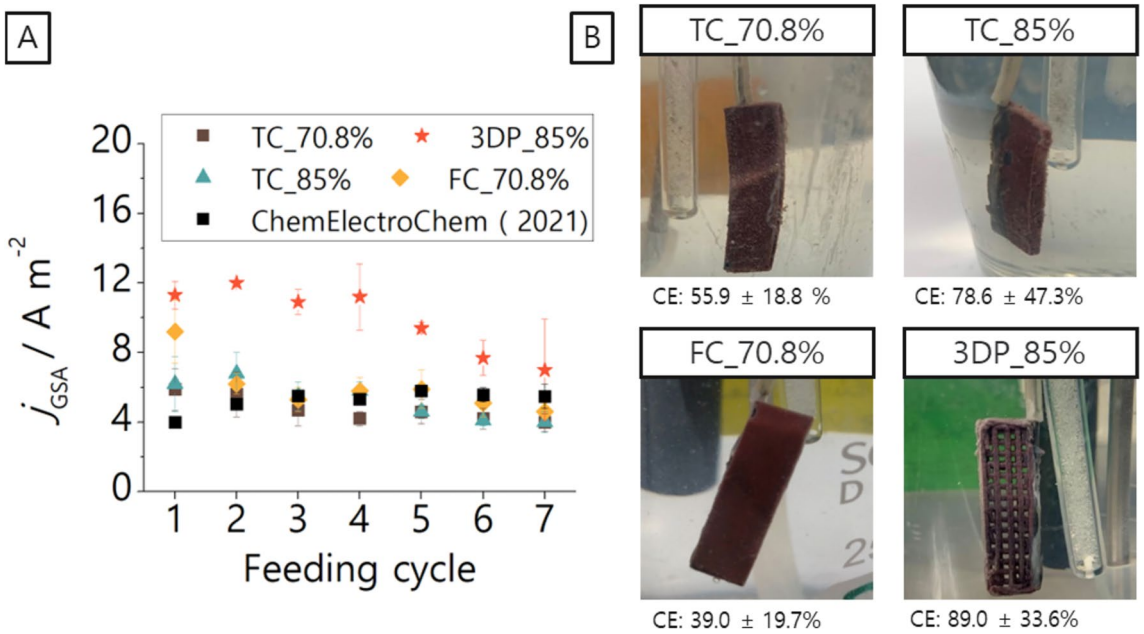

Fig. 5 **A** Maximum current density related to the geometric surface area (j_{GSA}) during chronoamperometry at + 0.2 V vs. Ag/AgCl sat. KCl at seven different feeding cycles and **B** Eye-visible formation of the reddish biofilm after 32 days of operation. The error bars on the figure on the left represent the standard deviation of the mean value for triplicates (n = 3, S.D.)

determined straightforward. He et al. indirectly estimated the electroactive area of the anode from the measurement of the highest peak current density during cyclic voltammetry [15]. Chen et al. used cardboard with well-defined geometry as the anode and calculated the total geometric surface area (including area from the structure, like GSA-CT in this work) using trigonometry-based approximation method validated with digital photography [19]. You et al. [22] and Kracke et. al [63] calculated the total geometric surface area from the electrode design in 3D CAD software. Furthermore, other works still consider the projected/geometric surface area with a vernier caliper and do not consider the internal surface area (as GSA-CT is calculated in this work) [20, 64]. In the material science community [65–68], the total geometric surface area is often acquired from 3D objects reconstructed from CT scans (GSA-CT). To broaden and enrich the discussion in microbial electrochemistry and technology, we here calculate GSA-CT and the volume of anodes (volume-CT) by reconstructing the CT scan. It is worth mentioning that only pore diameter larger than 30 µm were resolved by µCT, and regions with smaller pore size appear as dense material in the filtered image. Therefore, the effect of anode surface roughness has already been discussed separately in this article. When normalizing the current density by GSA-CT, the current density of the anode 3DP_85% (j_{GSA} 12.0 ± 1.2 A m^{-2}) falls to $j_{GSA\text{-}CT}$ of 4.9 ± 0.4 A m^{-2}, close to the range of j_{GSA} values reached by the others anodes. The anode 3DP_85% has almost the same GSA of its flat counterpart TC_85%. However, when considering the internal grid structure of 3DP_85%, its volume-CT of 0.276 cm^3 it is less than the volume-CT from TC_85% (0.439 cm^3), which could translate into a higher volumetric current density using less material. When benchmarking the anodes studied here with other works that also used *Geobacter* spp. biofilms [30], the anode 3DP_85% shows j_{GSA} higher than split-gold anodes and within the range of other metal anodes [69]. The tape-cast anodes (TC_85% and TC_70.8%) do not show substantial improvements to j_{GSA} and FC only improved j_{GSA} on short-term.

Biofilm and microbial community analysis and spatial distribution

After BES operation, the biofilm formed on the surface of the anodes was analyzed by SEM. Figure 6 shows images of the cross-section and the top view of the anodes and confirms the presence of a uniform and dense biofilm with a thickness ranging from 20 to 40 µm. However, due to the pore size of the anode surface, which is less than 6 µm, the biofilm does not grow within the pore structure. Nevertheless, the anode surface shows good biocompatibility.

The eye-visible reddish biofilm formed homogeneously on the surface of all anodes (Fig. 5B) indicates the predominant presence of *Geobacter* spp. (accession number on [39]). The microbial community composition was analyzed by the TRFLP analysis to verify any influence of the anode materials on the EAM. Based on the 16S rRNA gene of bacteria, the bacterial community of all anodes shows a low diversity

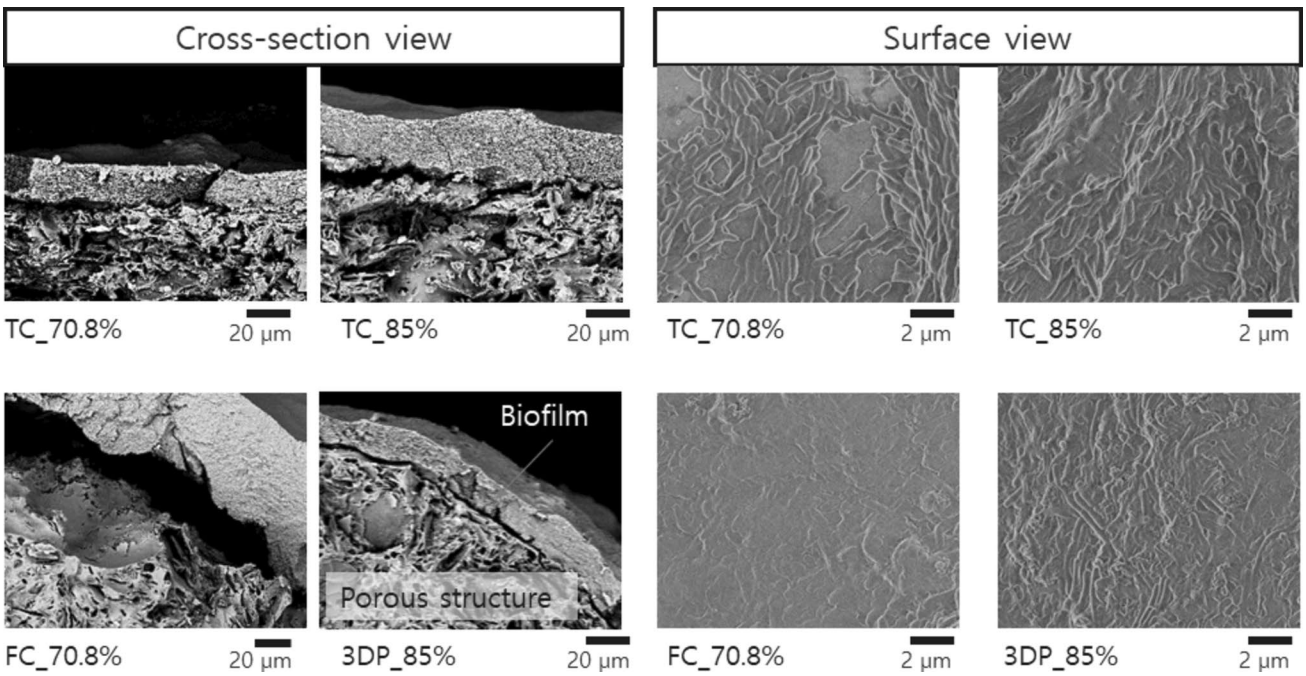

Fig. 6 SEM images of the dried biofilms after 28 days of operation from the cross-section and the top of the anodes

being dominated by the terminal restriction fragment (TRF) 213 bp (Fig. 7A) with a relative amplicon abundance ranging from 89.2 ± 2.7% for TC_85% to 96.5 ± 6.3% for FC_70.8%.

TRF 213 bp can be assigned to *Geobacter* spp. [39, 70] whose dominance is typical for the enrichment in BES with acetate as the sole carbon and energy source [71–73], and thus these are mainly responsible for EET processes. The methanogenic community (Fig. 7B) also shows a low diversity based on the *mcrA* gene. The TRFLP analysis of the methanogenic community revealed the dominance of TRF 228, which is attributed to *Methanomassiliicoccaceae* spp. with an abundance of 84.2 ± 12.6% for FC 70.8% up to 100% for TC_70.8% and TC_85%. Other TRFs like 437 for *Methanobacteriaceae* only play a minor role. Due to the very low concentration of the amplified *mcrA* gene compared to the 16S rRNA gene of bacteria (50–100 fold lower, data not shown), it seems to be that methanogenic archaea do not have a strong influence on the overall microbial community structure.

Conclusion

SiOC-based anodes with the same material composition and thus the same physicochemical properties were produced by tape-casting, freeze-casting, and direct-ink writing using different mass fractions of a slurry containing mainly poly(silsesquioxanes), graphite, and carbon black. The anodes showed significantly different texturing of the inner pore structure, pore and surface sizes; and surface roughness. The BES performance and the microbial community composition of these new anodes were studied. By adjusting the mass fraction of the slurry to 85 wt%, it was possible to develop a slurry with thixotropic behavior and a yield stress of 1141 Pa. This slurry was used to 3D-print the anode 3DP_85% with quasi-perfect grid structure (Pr_i factor 1.00 ± 0.28). The ceramic conversion of PDCs intrinsically generated pore sizes between 0.008 to 1 µm. Freeze casting a more dilute slurry of 70.8 wt% of mass fraction can produce anodes with additional pores larger than 1 µm on the surface, which act as surface roughness. The shape of these pores on the surface translates into "spikier" surface roughness and, hence, higher kurtosis up to 5.7. Besides, tape-casting and direct-ink writing involve high stress and create anodes with an internal pore structure with highly aligned particles but with closed porosity on the surface. However, the surface roughness of the anode FC_70.8% is only beneficial in the short term due to the effective growth of the biofilm. After the first cycle, the j_{GSA} drops steeply due to the pore-clogging of the surface. The pores created by direct-ink writing, which are larger than 1 mm, and the inherently larger total geometric surface area of the 3DP_85% anode prevents pore clogging and create more space for EAM colonization, as reflected in the highest j_{GSA} of around 12 A m^{-2}. When calculating the current density over the total geometric surface area determined by CT, the current density values drop by half and fall into the range of tape-cast and freeze-cast anodes. Nevertheless, the 3D-printed anodes have a higher volumetric current density and lead to a cost and mass reduction in the production of

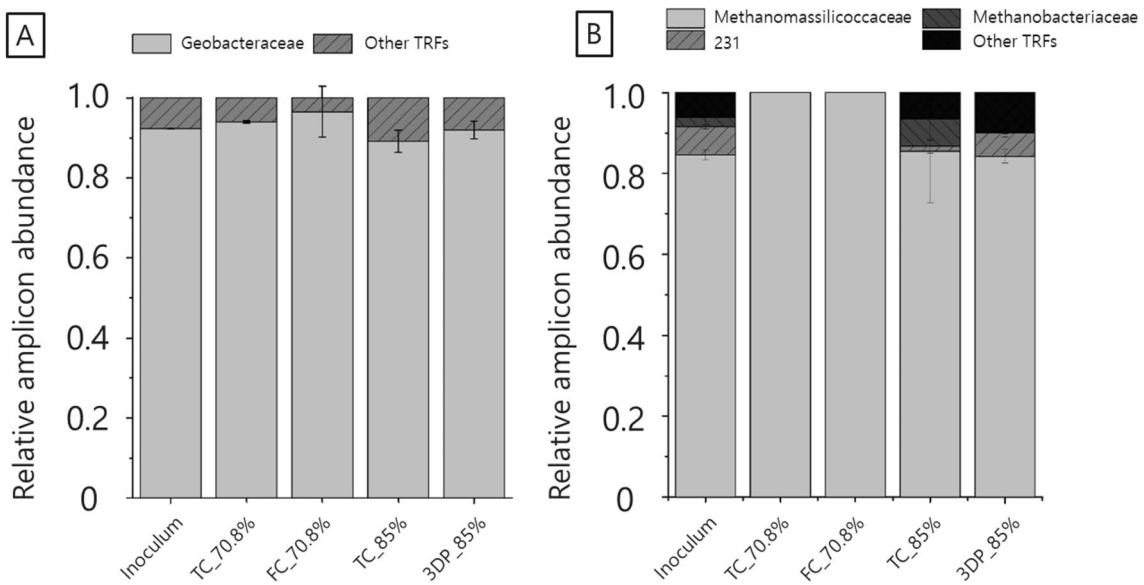

Fig. 7 Microbial community composition **A** bacterial community is dominated by TRF 213 representing *Geobacter* spp. in all BES regardless of the anode material. **B** Methanogenic community is dominated by *Methanomassiliicoccaceae* represented by TRF 228 and 236. The relative abundance refers to all sequences in each sample but only TRF with a contribution of more than 5% are displayed

electrodes. Finally, microbial community analysis confirmed the dominant presence of *Geobacter* spp. in the biofilm. In the future, the pores on the surface of the anodes could be enlarged to values higher than 20 µm by using sacrificial templates (e.g., PMMA) to allow colonization of the EAM within this pore structure and further increase j_{GSA}. A further step could be in vivo monitoring development and spatially resolved performance of biofilm anodes over time. This can be achieved using methods already established in the literature such as confocal Raman microscopy, optical coherence tomography or MR imaging.

Supplementary Information The online version contains supplementary material available at https://doi.org/10.1007/s40243-023-00253-4.

Acknowledgements This work was supported by German Research Foundation (DFG) within the Research Training Group GRK 1860 'Micro-, meso- and macroporous nonmetallic Materials: Fundamentals and Applica- tions' (MIMENIMA) and by the Helmholtz-Association in the frame of the Integration Platform "Tapping nature's potential for sustainable production and a healthy environment" at the UFZ

Funding Open Access funding enabled and organized by Projekt DEAL.

Declarations

Conflict of interest On behalf of all authors, the corresponding author states that there is no conflict of interest.

References

1. Hoang, A.T., Nižetić, S., Ng, K.H., Papadopoulos, A.M., Le, A.T., Kumar, S., Hadiyanto, H., Pham, V.V.: Microbial fuel cells for bioelectricity production from waste as sustainable prospect of future energy sector. Chemosphere **287**, 132285 (2022). https://doi.org/10.1016/j.chemosphere.2021.132285
2. Boas, J.V., Oliveira, V.B., Simões, M., Pinto, A.M.F.R.: Review on microbial fuel cells applications, developments and costs. J. Environ. Manag. **307**, 114525 (2022). https://doi.org/10.1016/j.jenvman.2022.114525
3. Ramya, M., Senthil Kumar, P.: A review on recent advancements in bioenergy production using microbial fuel cells. Chemosphere **288**, 132512 (2022). https://doi.org/10.1016/j.chemosphere.2021.132512
4. Borja-Maldonado, F., López Zavala, M.Á.: Contribution of configurations, electrode and membrane materials, electron transfer mechanisms, and cost of components on the current and future development of microbial fuel cells. Heliyon. **8**, e09849 (2022). https://doi.org/10.1016/j.heliyon.2022.e09849
5. Louro, R.O., Costa, N.L., Fernandes, A.P., Silva, A. V., Trindade, I.B., Fonseca, B.M., Paquete, C.M.: Chapter 2.2—Exploring the molecular mechanisms of extracellular electron transfer for harnessing reducing power in METs: methodologies and approaches, In: Mohan, S.V., Varjani, S., Pandey, A.B.T.-M.E.T. (eds.) Biomass, Biofuels Biochemistry pp. 261–293 Elsevier, London (2019). https://doi.org/10.1016/B978-0-444-64052-9.00010-8.
6. Heydorn, R.L., Engel, C., Krull, R., Dohnt, K.: Strategies for the targeted improvement of anodic electron transfer in microbial fuel cells. ChemBioEng. Rev. **7**, 4–17 (2020). https://doi.org/10.1002/cben.201900023
7. Chung, T.H., Dhar, B.R.: A mini-review on applications of 3D printing for microbial electrochemical technologies. Front. Energy Res. **9**, 1–8 (2021). https://doi.org/10.3389/fenrg.2021.679061
8. Zhai, J., Dong, S.: Recent advances in microbial fuel cell-based toxicity biosensors: strategies for enhanced toxicity response. Curr. Opin. Electrochem.Opin. Electrochem. **34**, 100975 (2022). https://doi.org/10.1016/j.coelec.2022.100975
9. Wei, J., Liang, P., Huang, X.: Recent progress in electrodes for microbial fuel cells. Bioresour. Technol. **102**, 9335–9344 (2011). https://doi.org/10.1016/j.biortech.2011.07.019
10. Zhao, F., Rahunen, N., Varcoe, J.R., Chandra, A., Avignone-Rossa, C., Thumser, A.E., Slade, R.C.T.: Activated carbon cloth as anode for sulfate removal in a microbial fuel cell. Environ. Sci. Technol. **42**, 4971–4976 (2008). https://doi.org/10.1021/es8003766
11. Dumas, C., Mollica, A., Féron, D., Basséguy, R., Etcheverry, L., Bergel, A.: Marine microbial fuel cell: use of stainless steel electrodes as anode and cathode materials. Electrochim. Acta. Acta **53**, 468–473 (2007). https://doi.org/10.1016/j.electacta.2007.06.069
12. Urania, M., ter Annemiek, H., et al.: Microbial communities and electrochemical performance of titanium-based anodic electrodes in a microbial fuel cell. Appl. Environ. Microbiol.Microbiol. **77**, 1069–1075 (2011). https://doi.org/10.1128/AEM.02912-09
13. Yaqoob, A.A., Ibrahim, M.N.M., Rafatullah, M., Chua, Y.S., Ahmad, A., Umar, K.: Recent advances in anodes for microbial fuel cells: an overview. Materials (Basel) **13**, 1–27 (2020). https://doi.org/10.3390/ma13092078
14. He, Y., Yang, J., Fu, Q., Li, J., Zhang, L., Zhu, X., Liao, Q.: Structure design of 3D hierarchical porous anode for high performance microbial fuel cells: from macro-to micro-scale. J. Power. Sources **516**, 230687 (2021). https://doi.org/10.1016/j.jpowsour.2021.230687
15. He, Y.T., Fu, Q., Pang, Y., Li, Q., Li, J., Zhu, X., Lu, R.H., Sun, W., Liao, Q., Schröder, U.: Customizable design strategies for high-performance bioanodes in bioelectrochemical systems. IScience (2021). https://doi.org/10.1016/j.isci.2021.102163
16. Chong, P., Erable, B., Bergel, A.: Effect of pore size on the current produced by 3-dimensional porous microbial anodes: a critical review. Bioresour. Technol.. Technol. (2019). https://doi.org/10.1016/j.biortech.2019.121641
17. Moß, C., Behrens, A., Schröder, U.: The limits of three-dimensionality: systematic assessment of effective anode macrostructure dimensions for mixed-culture electroactive biofilms. Chemsuschem (2019). https://doi.org/10.1002/cssc.201902923
18. Chen, S., Patil, S.A., Brown, R.K., Schröder, U.: Strategies for optimizing the power output of microbial fuel cells: transitioning from fundamental studies to practical implementation. Appl. Energy **233–234**, 15–28 (2019). https://doi.org/10.1016/j.apenergy.2018.10.015
19. Chen, S., He, G., Liu, Q., Harnisch, F., Zhou, Y., Chen, Y., Hanif, M., Wang, S., Peng, X., Hou, H., Schröder, U.: Layered

corrugated electrode macrostructures boost microbial bioelectrocatalysis. Energy Environ. Sci. **5**, 9769–9772 (2012). https://doi.org/10.1039/c2ee23344d
20. Bian, B., Wang, C., Hu, M., Yang, Z., Cai, X., Shi, D., Yang, J.: Application of 3D printed porous copper anode in microbial fuel cells. Front. Energy Res. **6**, 1–9 (2018). https://doi.org/10.3389/fenrg.2018.00050
21. Zhou, Y., Tang, L., Liu, Z., Hou, J., Chen, W., Li, Y., Sang, L.: A novel anode fabricated by three-dimensional printing for use in urine-powered microbial fuel cell. Biochem. Eng. J. **124**, 36–43 (2017). https://doi.org/10.1016/j.bej.2017.04.012
22. You, J., Fan, H.: Complete microbial fuel cell fabrication using additive layer manufacturing. Molecules **25**, 1–12 (2020)
23. Champigneux, P., Delia, M.L., Bergel, A.: Impact of electrode micro- and nano-scale topography on the formation and performance of microbial electrodes. Biosens. Bioelectron. **118**, 231–246 (2018). https://doi.org/10.1016/j.bios.2018.06.059
24. Kulchartvijit, T., Chianrabutra, C., Sukontasing, S., Chianrabutra, S.: The effects of surface roughness of the stainless-steel anode on electricity enhancement of microbial fuel cell. Trends Sci. (2022). https://doi.org/10.48048/tis.2022.3680
25. Champigneux, P., Renault-Sentenac, C., Bourrier, D., Rossi, C., Delia, M.L., Bergel, A.: Effect of surface roughness, porosity and roughened micro-pillar structures on the early formation of microbial anodes. Bioelectrochemistry **128**, 17–29 (2019). https://doi.org/10.1016/j.bioelechem.2019.03.002
26. Shao, G., Hanaor, D.A.H., Shen, X., Gurlo, A.: Freeze casting: From low-dimensional building blocks to aligned porous structures—A review of novel materials, methods, and applications. Adv. Mater. **32**, 1907176 (2020). https://doi.org/10.1002/adma.201907176
27. Chadha, U., Selvaraj, S.K., Ravinuthala, A.K., Maddini, Y., Arasu, K., Yadav, S., Kumari, O., Pant, S., Paramasivam, V.: Bioinspired techniques in freeze casting: a survey of processes, current advances, and future directions. Int. J. Polym. Sci. (2022). https://doi.org/10.1155/2022/9169046
28. Condi Mainardi, J., Bonini Demarchi, C., Mirdrikvand, M., Karim, M.N., Dreher, W., Rezwan, K., Maas, M.: 3D bioprinting of hydrogel/ceramic composites with hierarchical porosity. J. Mater. Sci. **57**, 3662–3677 (2022). https://doi.org/10.1007/s10853-021-06829-7
29. Zhang, F., Li, Z., Xu, M., Wang, S., Li, N., Yang, J.: A review of 3D printed porous ceramics. J. Eur. Ceram. Soc. **42**, 3351–3373 (2022). https://doi.org/10.1016/j.jeurceramsoc.2022.02.039
30. da Rosa Braun, P.H., Canuto de Almeida e Silva, T., Rodrigo Quejigo, J., Kuchenbuch, A., Rezwan, K., Harnisch, F., Wilhelm, M.: Impact of surface properties of porous SiOC-based materials on the performance of Geobacter biofilm anodes. ChemElectroChem **8**, 850–857 (2021). https://doi.org/10.1002/celc.202001568
31. Fontão, N.C., Ferrari, L.N., Sapatieri, J.C., Rezwan, K., Wilhelm, M.: Influence of the pyrolysis temperature and TiO_2-incorporation on the properties of SiOC/SiC composites for efficient wastewater treatment applications. Membranes (Basel) (2022). https://doi.org/10.3390/membranes12020175
32. Arai, N., Faber, K.T.: Gradient-controlled freeze casting of preceramic polymers. J. Eur. Ceram. Soc. **43**, 1904–1911 (2023). https://doi.org/10.1016/j.jeurceramsoc.2022.12.016
33. Lyu, Z., Koh, J.J., Lim, G.J.H., Zhang, D., Xiong, T., Zhang, L., Liu, S., Duan, J., Ding, J., Wang, J., Wang, J., Chen, Y., He, C.: Direct ink writing of programmable functional silicone-based composites for 4D printing applications. Interdiscip. Mater. **1**, 507–516 (2022). https://doi.org/10.1002/idm2.12027
34. Moni, P., Deschamps, A., Schumacher, D., Rezwan, K., Wilhelm, M.: A new silicon oxycarbide based gas diffusion layer for zinc-air batteries. J. Colloid Interface Sci. **577**, 494–502 (2020). https://doi.org/10.1016/j.jcis.2020.05.041
35. Colombo, P., Gambaryan-Roisman, T., Scheffler, M., Buhler, P., Greil, P.: Conductive ceramic foams from preceramic polymers. J. Am. Ceram. Soc. **84**, 2265–2268 (2001). https://doi.org/10.1111/j.1151-2916.2001.tb01000.x
36. Viard, A., Fonblanc, D., Lopez-Ferber, D., Schmidt, M., Lale, A., Durif, C., Balestrat, M., Rossignol, F., Weinmann, M., Riedel, R., Bernard, S.: Polymer derived Si–B–C–N ceramics: 30 years of research. Adv. Eng. Mater. (2018). https://doi.org/10.1002/adem.201800360
37. Stabler, C., Ionescu, E., Graczyk-Zajac, M., Gonzalo-Juan, I., Riedel, R.: Silicon oxycarbide glasses and glass-ceramics: "all-rounder" materials for advanced structural and functional applications. J. Am. Ceram. Soc. **101**, 4817–4856 (2018). https://doi.org/10.1111/jace.15932
38. Canuto de Almeida e Silva, T., Fernandes Kettermann, V., Pereira, C., Simões, M., Wilhelm, M., Rezwan, K.: Novel tape-cast SiOC-based porous ceramic electrode materials for potential application in bioelectrochemical systems. J. Mater. Sci. **54**, 6471–6487 (2019). https://doi.org/10.1007/s10853-018-03309-3
39. Harnisch, F., Koch, C., Patil, S.A., Hübschmann, T., Müller, S., Schröder, U.: Revealing the electrochemically driven selection in natural community derived microbial biofilms using flow-cytometry. Energy Environ. Sci. **4**, 1265–1267 (2011). https://doi.org/10.1039/c0ee00605j
40. da Rosa Braun, P.H., Rezwan, K., Wilhelm, M.: Impact of a tert-butyl alcohol-cyclohexane system used in unidirectional freeze-casting of SiOC on compressive strength and mass transport. Mater. Des. **212**, 110186 (2021). https://doi.org/10.1016/j.matdes.2021.110186
41. Schneider, C.A., Rasband, W.S., Eliceiri, K.W.: NIH Image to ImageJ: 25 years of image analysis. Nat. Methods **9**, 671–675 (2012). https://doi.org/10.1038/nmeth.2089
42. Ouyang, L., Yao, R., Zhao, Y., Sun, W.: Effect of bioink properties on printability and cell viability for 3D bioplotting of embryonic stem cells. Biofabrication **8**, 1–12 (2016). https://doi.org/10.1088/1758-5090/8/3/035020
43. Schwab, A., Levato, R., D'Este, M., Piluso, S., Eglin, D., Malda, J.: Printability and shape fidelity of bioinks in 3D bioprinting. Chem. Rev. **120**, 11028–11055 (2020). https://doi.org/10.1021/acs.chemrev.0c00084
44. Kikinis, R., Pieper, S.D., Vosburgh, K.G.: 3D slicer: a platform for subject-specific image analysis, visualization, and clinical support BT—intraoperative imaging and image-guided therapy. In: Jolesz, F.A. (ed.), pp. 277–289. Springer, New York (2014). https://doi.org/10.1007/978-1-4614-7657-3_19.
45. Duboust, N., Ghadbeigi, H., Pinna, C., Ayvar-Soberanis, S., Collis, A., Scaife, R., Kerrigan, K.: An optical method for measuring surface roughness of machined carbon fibre-reinforced plastic composites. J. Compos. Mater. **51**, 289–302 (2017). https://doi.org/10.1177/0021998316644849
46. Kundrak, J., Gyani, K., Bana, V.: Roughness of ground and hard-turned surfaces on the basis of 3D parameters. Int. J. Adv. Manuf. Technol. **38**, 110–119 (2008). https://doi.org/10.1007/s00170-007-1086-9
47. Kim, J.R., Min, B., Logan, B.E.: Evaluation of procedures to acclimate a microbial fuel cell for electricity production. Appl. Microbiol. Biotechnol. **68**, 23–30 (2005). https://doi.org/10.1007/s00253-004-1845-6
48. Gimkiewicz, C., Harnisch, F.: Waste water derived electroactive microbial biofilms: growth, maintenance, and basic characterization. J. Vis. Exp. (2013). https://doi.org/10.3791/50800
49. Weisburg, W.G., Barns, S.M., Pelletier, D.A., Lane, D.J.: 16S ribosomal DNA amplification for phylogenetic study. J. Bacteriol.

173, 697–703 (1991). https://doi.org/10.1128/jb.173.2.697-703.1991
50. Steinberg, L.M., Regan, J.M.: Phylogenetic comparison of the methanogenic communities from an acidic, oligotrophic fen and an anaerobic digester treating municipal wastewater sludge. Appl. Environ. Microbiol. (2008). https://doi.org/10.1128/AEM.00553-08
51. Koch, C., Popiel, D., Harnisch, F.: Functional redundancy of microbial anodes fed by domestic wastewater. ChemElectroChem **1**, 1923–1931 (2014). https://doi.org/10.1002/celc.201402216
52. Koch, C., Kuchenbuch, A., Kretzschmar, J., Wedwitschka, H., Liebetrau, J., Müller, S., Harnisch, F.: Coupling electric energy and biogas production in anaerobic digesters-impacts on the microbiome. RSC Adv. (2015). https://doi.org/10.1039/c5ra03496e
53. Nishihora, R.K., Quadri, M.G.N., Hotza, D., Rezwan, K., Wilhelm, M.: Tape casting of polysiloxane-derived ceramic with controlled porosity and surface properties. J. Eur. Ceram. Soc. **38**, 4899–4905 (2018). https://doi.org/10.1016/j.jeurceramsoc.2018.07.016
54. Drillet, J.-F., Adam, M., Barg, S., Herter, A., Koch, D., Schmidt, V., Wilhelm, M.: Development of a novel zinc/air fuel cell with a Zn foam anode, a PVA/KOH membrane and a MnO2/SiOC-based air cathode. ECS Trans. **28**, 13–24 (2010). https://doi.org/10.1149/1.3507923
55. Jabbari, M., Bulatova, R., Tok, A.I.Y., Bahl, C.R.H., Mitsoulis, E., Hattel, J.H.: Ceramic tape casting: a review of current methods and trends with emphasis on rheological behaviour and flow analysis. Mater. Sci. Eng. B Solid-State Mater. Adv. Technol. **212**, 39–61 (2016). https://doi.org/10.1016/j.mseb.2016.07.011
56. del-Mazo-Barbara, L., Ginebra, M.P.: Rheological characterisation of ceramic inks for 3D direct ink writing: A review. J. Eur. Ceram. Soc. **41**, 18–33 (2021). https://doi.org/10.1016/j.jeurceramsoc.2021.08.031
57. Naviroj, M., Voorhees, P.W., Faber, K.T.: Suspension- and solution-based freeze casting for porous ceramics. J. Mater. Res. **32**, 3372–3382 (2017). https://doi.org/10.1557/jmr.2017.133
58. Hirao, K., Ohashi, M., Brito, M.E., Kanzaki, S.: Processing strategy for producing highly anisotropic silicon nitride. J. Am. Ceram. Soc. **78**, 1687–1690 (1995). https://doi.org/10.1111/j.1151-2916.1995.tb08871.x
59. Gong, S., Zhu, Z.H., Meguid, S.A.: Anisotropic electrical conductivity of polymer composites with aligned carbon nanotubes. Polymer (Guildf) **56**, 498–506 (2015). https://doi.org/10.1016/j.polymer.2014.11.038
60. Massaglia, G., Quaglio, M.: 3D composite PDMS/MWCNTs aerogel as high-performing anodes in microbial fuel cells. Nanomaterials (2022). https://doi.org/10.3390/nano12234335
61. Yang, K., Shi, J., Wang, L., Chen, Y., Liang, C., Yang, L., Wang, L.N.: Bacterial anti-adhesion surface design: surface patterning, roughness and wettability: a review. J. Mater. Sci. Technol. **99**, 82–100 (2022). https://doi.org/10.1016/j.jmst.2021.05.028
62. Carmona-Martínez, A.A., Lacroix, R., Trably, E., Da Silva, S., Bernet, N.: On the actual anode area that contributes to the current density produced by electroactive biofilms. Electrochim. Acta **259**, 395–401 (2018). https://doi.org/10.1016/j.electacta.2017.10.200
63. Kracke, F., Deutzmann, J.S., Jayathilake, B.S., Pang, S.H., Chandrasekaran, S., Baker, S.E., Spormann, A.M.: Efficient hydrogen delivery for microbial electrosynthesis via 3D-printed cathodes. Front. Microbiol. **12**, 1–11 (2021). https://doi.org/10.3389/fmicb.2021.696473
64. Bian, B., Shi, D., Cai, X., Hu, M., Guo, Q., Zhang, C., Wang, Q., Sun, A.X., Yang, J.: 3D printed porous carbon anode for enhanced power generation in microbial fuel cell. Nano Energy **44**, 174–180 (2018). https://doi.org/10.1016/j.nanoen.2017.11.070
65. Reedy, C.L., Reedy, C.L.: High-resolution micro-CT with 3D image analysis for porosity characterization of historic bricks. Herit. Sci. **10**, 1–22 (2022). https://doi.org/10.1186/s40494-022-00723-4
66. Lai, P., Moulton, K., Krevor, S.: Pore-scale heterogeneity in the mineral distribution and reactive surface area of porous rocks. Chem. Geol. **411**, 260–273 (2015). https://doi.org/10.1016/j.chemgeo.2015.07.010
67. Behnsen, J.G., Black, K., Houghton, J.E., Worden, R.H.: A review of particle size analysis with X-ray CT. Materials (Basel) **16**, 1–17 (2023). https://doi.org/10.3390/ma16031259
68. Kuhlmann, K., Sinn, C., Siebert, J.M.U., Wehinger, G., Thöming, J., Pesch, G.R.: From µCT data to CFD: an open-source workflow for engineering applications. Eng. Appl. Comput. Fluid Mech. **16**, 1706–1723 (2022). https://doi.org/10.1080/19942060.2022.2109758
69. Baudler, A., Schmidt, I., Langner, M., Greiner, A., Schröder, U.: Does it have to be carbon? Metal anodes in microbial fuel cells and related bioelectrochemical systems. Energy Environ. Sci. **8**, 2048–2055 (2015). https://doi.org/10.1039/c5ee00866b
70. Korth, B., Kretzschmar, J., Bartz, M., Kuchenbuch, A., Harnisch, F.: Determining incremental coulombic efficiency and physiological parameters of early stage *Geobacter* spp. enrichment biofilms. PLoS ONE (2020). https://doi.org/10.1371/journal.pone.0234077
71. Commault, A.S., Lear, G., Packer, M.A., Weld, R.J.: Influence of anode potentials on selection of *Geobacter* strains in microbial electrolysis cells. Bioresour. Technol. **139**, 226–234 (2013). https://doi.org/10.1016/j.biortech.2013.04.047
72. Zhu, X., Yates, M.D., Hatzell, M.C., Ananda Rao, H., Saikaly, P.E., Logan, B.E.: Microbial community composition is unaffected by anode potential. Environ. Sci. Technol. **48**, 1352–1358 (2014). https://doi.org/10.1021/es404690q
73. Torres, C.I., Krajmalnik-Brown, R., Parameswaran, P., Marcus, A.K., Wanger, G., Gorby, Y.A., Rittmann, B.E.: Selecting anode-respiring bacteria based on anode potential: phylogenetic, electrochemical, and microscopic characterization. Environ. Sci. Technol. **43**, 9519–9524 (2009). https://doi.org/10.1021/es902165y